Title

Ag+/Li+ Ion-Exchange in LLZTO to Introduce Surface Layer Compressive Stress and Improve Electrochemical Performance

Journal

ECS Meeting Abstracts, MA2024-02(10)

ISSN

2151-2043

Authors

Morris, Sydney
Jagad, Harsh
Harris, Stephen J
et al.

Publication Date

2024-11-22

DOI

10.1149/ma2024-02104876mtgabs

Peer reviewed

Ion size effects on the thermodynamic, kinetic, and mechanical properties during ion exchange in solid-state electrolytes

Harsh D. Jagad [1], Stephen J. Harris [2], Brian W. Sheldon [1], Yue Qi [1*]

[1] School of Engineering, Brown University, 184 Hope Street, Providence, Rhode Island, United States of America

[2] Materials Science Division, Lawrence Berkeley National Lab, 1 Cyclotron Road, Berkeley, California 94720, United States of America

Abstract

Ion exchange offers a pathway to impose residual compressive stresses to mitigate the electro-chemo-mechanical cracking of solid-state electrolytes such as Lithium Lanthanum Zirconium Oxide. This study uses a coupled multiscale framework—integrating Density Functional Theory (DFT), Molecular Dynamics (MD), and Continuum modeling—to examine how exchange ion size influences stress, diffusion, and fracture toughness and electronic properties. Larger isovalent ions (Na^+, Ag^+, K^+) were exchanged with Li^+, with DFT confirming their preference for octahedral 96h sites and a linear relationship between ion size and chemical free expansion coefficient. MD simulations reveal stress and concentration effects on exchange ion diffusivity, with Na^+ and Ag^+ maintaining favorable mobility while K^+ shows concentration dependent clustering. Continuum modeling predicts the range of fracture strength improvements and required exchanged ion concentration profile. It was shown that a 3.33-fold improvement in fracture strength for 20 μm cracks with 1 GPa surface stress is achievable with 7% of the smaller Na^+ or 4.5% with the larger Ag^+ concentration on [near?] the surface after similar diffusion time. On the other hand, larger exchanged ions ~~penalizes~~penalize Li^+ diffusivity by increasing the activation volume and activation energy. Interestingly, Na^+ has a negligible penalty the Li ion diffusivity. The Li ion diffusivity is ~~reduces~~ reduced by ~40% with Ag^+ ion exchange. The electronic band structure analysis shows no size dependent change in the bandgap, though Ag^+ introduces localized defect states near the valence band maximum. This study highlights ion size as a key factor in optimizing LLZO properties, offering a framework to improve solid-state battery performance.

*Corresponding Author Email: yueqi@brown.edu

1: Introduction

The oxide based $Li_7La_3Zr\square_2O_{12}$ (LLZO) is a unique solid state electrolyte material for solid state batteries, with high ionic conductivity [1, 2], stability against Li metal [3, 4] and a wide electronic bandgap [5, 6]. Yet, when LLZO is paired with Li metal anode, Li metal filaments penetrate and mechanically crack the LLZO [7-12]. It has been demonstrated by various experiments and modeling that cracking at the LLZO/lithium metal anode is electro-chemo-mechanically coupled [13-15] by several factors that can accelerate the Li filament growth. ~~The~~ eElectronic conductivity is provided by ~~the~~ electron density on ~~the~~ preexisting ~~surface~~ surface-type defects, including ~~pore~~ surface pores, grain boundaries, surface flaws, ~~as well as~~and newly formed crack surfaces~~, etc~~. [5, 10] This electron density is trapped on La-ions ~~of~~ in these defects, which can reduce Li^+-ions to metallic lithium~~–~~, causing metallic lithium filament ~~forming~~ formation inside ~~of~~ LLZO. These metallic filaments can attract lithium flux, causing continuous growth, and this can lead to tensile back stress in the LLZO [13, 16]. These tensile stresses in the LLZO can cause existing flaws, especially the mechanically weaker surface type of defects~~,~~ that inevitably exist, to propagate as cracks.

In previous works we proposed inducing surface residual compressive in-plane stresses as an amelioration strategy to resist surface crack propagation and tackle this coupled degradation mechanism [17, 18]. (Residual stresses are stresses that remain in a material when all outside loadings are removed.] The level of macroscopic stress to deflect crack propagation is likely to be on the order of 200 MPa, as demonstrated by Fincher *et al,* who engineered biaxial mechanical loads in a $Li_{6.6}La_3Zr_{1.6}Ta_{0.4}O_{12}$ (LLZTO) sample [12], although the loading conditions are different from the proposed surface residual compressive stress. Recently Xin *et al,* have shown that nanoscale doping of Ag on LLZTO caused subsurface Li/Ag ion exchange up to 50 nm and resisted larger nanoindentation force up to 5 times, suggesting the effectiveness of surface modification on crack resistance [19]. Several methods, including ion implantation and ion exchange, were discussed by Qi *et al.* [17] to induce surface residual compressive stress.

Recently, ~~the~~ ion ~~implantation~~ implantation-induced stress~~es~~ was reported by several experimental groups. Yao *et al,* used Xe implantation up to a depth of 60-70 nm in LLZTO, in which they claimed compressive stress ~3 to 20 GPa [20] was generated, depending on the dosage

of Xe. Flatshcer *et al*, ion implanted Ag in LLZTO up to a depth of 1 μm and generated a compressive stress of ~700MPa, which was able to deflect nano-indented cracks parallel to the surface. However, the ion implantation created an amorphization depth ~650 to 700 nm [21]. Thus ion-implantation may generate the required surface compressive stress, but ~~it has two limitations: insufficient~~the reported depths of compressive stress have been limited, and the surface may be ~~amorphization~~amorphized. [Chunmei has used MeV implantation to get several microns of depth, submitted.] A submicron surface compression layer may be inadequate because it is less than the typical grain size in LLZO [22], as the grain boundaries can be viewed as an intrinsic flaw in LLZO due to their lower strength than the single grained LLZO [23]. The amorphization in the ion implanted region due to the bombardment of high energy foreign ions on the lattice ~~hinders~~ may hinder the ionic conductivity of Li^+, which manifests as large increase in impedance [20, 21]. [I'm toning down the criticism of other people's work.]

Unlike ion implantation, ion exchange can provide residual compressive stress without (or with minimal) amorphization [ref]. In previous work, we modeled the use of K^+ to induce residual compressive in LLZO using ion exchange with micron level depth [18]. Although the discussion of the depth level of ion exchange in solid state battery electrolytes is limited, this process has been explored in glasses extensively. In commercial glasses, ~~,~~ typically~~,~~ a high temperature (600K) molten salt precursor ~~approach is utilized that~~ generates diffusion-controlled concentration (and hence stress) profiles of the exchange ion, which can be tens to hundreds of microns thick. For example, Belostotsky exchanged Na^+ with K^+ using a molten KNO_3 salt for a depth of up to 35 microns [24]. Gy reported an exchange depth from 40 to 100 microns depending on the process time and temperature, with a peak compressive stress of 600 MPa [25]. Tyagi *et al*. ~~have~~ showed a Li^+/Na^+ exchange in mixed aluminosilicate glass, resulting in an exchange depth of 200 microns with a peak compressive stress of 1200 MPa [26]. The exchanged ion concentrations typically follow an error function, $erf\ (x)$, in these thermal diffusion processes. Electric fields can be used to enhance the ion exchange process in addition to thermal diffusion (called Field Assisted Ion Exchange) and to develop ~~almost~~ nearly uniform concentration profiles [27, 28, 29, 30]. An accurate ~~description~~ understanding of the concentration profile of the exchanged ion is necessary, as it dictates the stress profile in the solid electrolyte. Our previous work

assumed a shallow depth of ion exchange with no concentration gradient [18]. We show later in this article that while the uniform concentration model can predict reasonable concentration and stress profiles, it does not accurately capture the gain in the apparent fracture toughness.

We expect two distinct differences between ion exchange in glass vs. in crystalline LLZO. One is related to ion-exchange induced stress, and one is related to Li-ion conductivity. The expectation that larger ions would deliver larger residual compressive stress was not always met in glasses [30] [31], due to the high temperature viscoelastic stress relaxation of silicate network [31, 32]. Ion exchange in crystalline LLZO, may not face such relaxation limitations. LLZO can also tolerate much higher temperatures than glasses~~;~~, thus, it may be possible to capitalize on the high temperature diffusivity for the ion exchange process. ~~The s~~Stiff oxide based frameworks can still exhibit linear elastic mechanical responses [33] at the ion exchange temperature. Thus, it may be possible to engineer larger stresses by considering ions with larger sizes or larger concentrations. The diffusion of exchange ions in glasses has been well studied and exhibits the 'mixed alkali effect' [34, 35]. The mixed alkali effect refers to the fact that, on the one hand, exchanged ions exhibit concentration dependent diffusion coefficients, and on the other hand, the native ions show a decrease in their diffusion coefficient by an increase in activation energy [36]. This may not have a serious impact on application in glasses, as they are generally not expected to have fast ion conductivity. However, it can have a profound impact on materials like LLZO, ~~where the~~whose merit lies in its fast conduction of Li^+.

The goal of ion exchange is to "stuff" a larger ion in the subsurface region of the solid-state electrolyte at the solid electrolyte~~-~~anode interface to provide residual in-plane biaxial compression (as opposed to ~~.~~a stack pressure, which leads to an out-of-plane stress). Considering only isovalent cations that are larger than Li^+ [37], and excluding radioactive [38], toxic [39, 40] and expensive [41] cations, we will focus ~~the possible~~on ion exchange with Na^+, Ag^+, K^+ ~~to exchange with Li^+ in LLZO~~. Li^+ can occupy both tetrahedral and octahedral sites in LLZO. The Shannon radi~~us~~ for Li^+, Na^+, Ag^+ and K^+ ~~in the tetrahedral site is~~ are 0.59 Å, 0.99 Å, 1.00 Å and 1.37 Å, respectively in the tetrahedral sites; and they are ~~in the octahedral site is~~ 0.76 Å, 1.02 Å, 1.15 Å and 1.38 Å, respectively in the octahedral sites~~.~~ [37]. This suggests that Na^+, Ag^+ and K^+ are 68%, 69% and 132% larger than Li^+, if occupying the tetrahedral site; ~~or~~ and 34%, 51%,

and 81% larger in the octahedral site. Therefore, several key questions arise ~~on~~ with respect to the impact of ionic size effects: ~~. Which site~~ The site ~~will~~ they occupy; the variation of the chemical strain with the ion size ~~, ;~~ the appropriate exchanged ion concentration gradient to induce compressive stress on the order of ~200MPa; and ~~if~~ whether they ~~will~~ hinder Li^+ ion diffusion at room temperature ~~?~~.

Thus, it is necessary to holistically understand the thermo-kinetic-mechanical behavior of exchanged ions to optimize the residual stresses without penalizing the Li^+ transport. In the absence of experimental evidence, we relied on a fully self-consistent multiscale model framework to address these key questions about ion exchange in LLZO ~~by exchanging~~ Li^+ is exchanged with the larger isovalent ions Na^+, Ag^+ and K^+. The model ~~of~~ for macroscopic stress induced by the ion concentration gradient is similar to the diffusion induced stress (DIS) models for electrode materials [42-45] and ion-exchanged glasses [46]. Traditionally, these continuum models reply on fitting the diffusion coefficients and chemical strains to experimental measurements [46, 47] Qi *et al,* predicted Li concentration dependent elastic constants [48] and chemical strain [48] from density functional theory (DFT) calculations for the continuum DIS modeling [43] and showed better [better than what?] agreement with the in-situ strain maps in graphite electrodes [49] and single crystalline Ni-rich electrode particles [50]. These efforts motivated this work to develop a fully self-consistent multiscale ion exchange model coupling the chemical strain/stress with the diffusion coefficient, which can then be used to predict the exchange ion concentration profile and the fracture toughness increase.

2: Computational Methods

Figure 1 shows the flow chart of this fully self-consistent multiscale model framework, ~~integrating~~ which integrates different modeling approaches. At the atomic scale, DFT calculations (purple ~~outline~~ box in **Figure 1**) were performed to evaluate the site selectivity of the exchanged ions and determine the most stable configurations. The most stable configurations were then used to evaluate the ion-exchange formation energy, E_f, which is combined with other DFT results to screen various salt precursors to predict the feasible exchange ion salts. The effect

of ion exchange on the electronic properties and the chemical free expansion coefficients, γ, were also evaluated at the DFT level. γ includes the material's expansion due to physical factors, while excluding the effects of chemical interactions or reactions. [Is this correct? You should define what it means, since it's not a term everyone knows.] ~~The d~~Defect sampling also provided a dataset to train and finetune the force field used ~~in~~ for our molecular dynamics (MD) calculations. The MD simulations (red outline in **Figure 1**) [You also used a red line next to C_{IX}.] were used to ~~quantify~~ determine the diffusion coefficients of Li^+-ions, D_{Li}, and exchanged ions, D_{IX}. Both can be a function of temperature (T), stress (σ_c), and concentration of exchanged ions (C_{IX}). These predicted stress-concentration-coupled diffusion coefficients $D_{IX}(T, \sigma_C, C_{IX})$ and the chemical free expansion coefficient, γ, were used to develop a continuum level diffusion-induced-stress model for ion exchange at microscale (golden outline in **Figure 1**). The continuum level model was then used to understand the improvement in the apparent fracture strength of LLZO and to evaluate the risks of spontaneous fracture in LLZO.

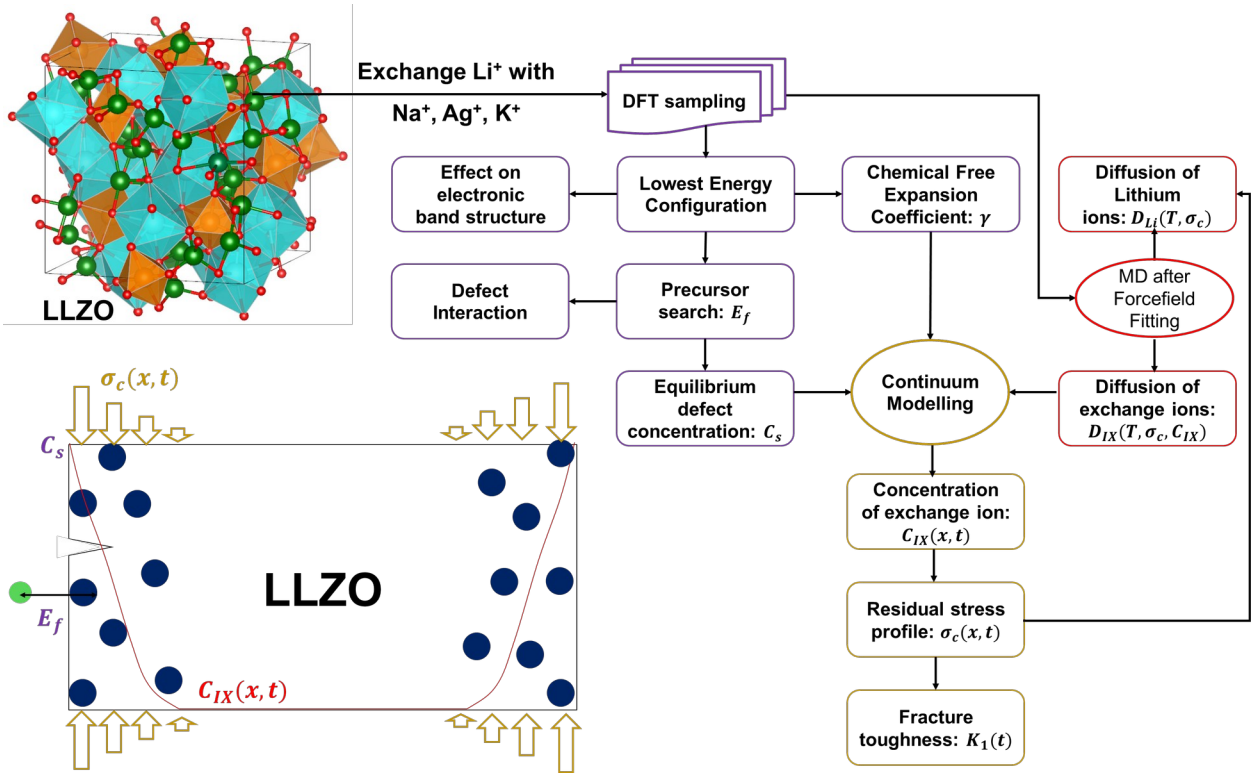

Figure 1: Computational framework of ion exchange in LLZO. The upper left panel shows the crystal structure of LLZO with La^{3+} in cyan polyhedron, Zr^{4+} in orange polyhedron and Li^{+} diffusional network shown in green with O^{2-} in red. The computational framework highlights the connection of DFT (purple outline) to MD (red outline) to continuum modelling (golden outline). The lower left panel is a schematic of two-sided ion exchange on a solid electrolyte with the navy spheres representing the exchange ions. The color scheme is shared with the computation framework, thus indicating the role of each modelling technique to capture the associated phenomenon.

2.1: Density Functional Theory Calculations

The cubic I-3m structure for $Li_7La_3Zr\square_2O_{12}$ was used with lattice parameter of 13.003 Å. The~~A~~ simulation box of LLZO has 8 formula units, thus $Li_{56}La_{24}Zr_{16}O_{96}$. The Li^{+} distribution was based on rules provided in~~set in~~ [5, 51-53]. All site sampling calculations were done using Density Functional Theory (DFT) in the Vienna Ab Initio Simulation Package (VASP) [54]. A plane wave basis set was chosen with the energy cutoff set to 600 eV. Electronic minimization was performed under the Generalized Gradient Approximation (GGA) with the exchange correlational functional of Perdew, Burke and Ezenhorf (PBE) [55] using a Gaussian smearing of 0.1 eV. The electronic convergence criterion was set to 10^{-5} eV, and the force criterion was set to 0.03 eV/Å per atom. A k-point density of 1x1x1 was used. For the electronic density of states (DOS) calculation, the electronic occupancy was based on the Tetrahedron method with a 2x2x2 Monkhorst Pack k-point mesh for higher accuracy.

Site sampling was conducted by exchanging 1 Li^{+} with 1 exchanged ion [Na^{+}, Ag^{+}, K^{+}], equivalent to a concentration $C_{IX}=1.7\%$ ~~of ion~~ exchanged ions. The ionic positions were first relaxed with fixed cell shape and size. To obtain the structure at higher concentrations, the minimum energy structure with 1.7% exchanged ion was used as the basis for further sampling at higher concentration. ($C_{IX}=3.4\%$ for 2 exchanges in the simulation cell). Similarly, for 5.1% concentration sampling, the 3.4% concentration was taken as the basis. Then the constrained DFT cells are fully relaxed in size and shape, as well as the ionic positions at various concentrations of IX species ($C_{IX}=$¿0%, 1.7%, 3.4%). [Fully relaxed? Shouldn't the bottom of the cell be held rigid to take into account the constraint created by the bulk?]

The defect formation energy of ion exchange when exchanging n Li^{+} with n cations ~~was~~ is written in the dilute limit as:

$$E_f = \frac{(E_{IX} - E_{bulk})}{n} + \Delta\mu_{Li} - \Delta\mu_{IX} \quad \text{(eq. 1)}$$

where E_{IX}, E_{bulk} refer to the 0K DFT energy of ~~the ion~~ ion-exchanged LLZO and bulk LLZO respectively, and $\Delta\mu_i$ refer to the change in the chemical potential of the species, $i = Li \vee IX$, ~~thus~~ depending on the anionic reference state. For a similar change in the anionic reference states (for example Li_2O vs Na_2O / Ag_2O / K_2O), the difference in the change in chemical potential between Li^+ and the exchange ion was approximated as $\Delta\mu_{Li} - \Delta\mu_{IX}$ $E_{Li}^{DFT} - E_{IX}^{DFT}$, where E_i^{DFT} is the energy per alkali species obtained from the Materials Project database [56]. [How good do you expect this approximation to be?] ~~The a~~Additional corrections necessary to obtain the temperature dependent "defect formation free energy" are provided in the Supplementary Information (SI).

Although each point defect induces a chemical strain "tensor", [why is tensor in quotes?] which can be calculated from DFT [57, 58], the average volume change due to the randomly distributed and oriented point defects can still be described by a scalar with isotropic chemical strains (ε_c) [59]. Therefore, the cub~~ic~~ root of the volume of the freely expanded cell corresponds to the freely expanded lattice constant 'a', which depends on the concentration C_{IX}. The chemical free expansion coefficient (γ) is defined as the ratio of chemical strain (ε_c) ~~with the~~to C_{IX}.

$$\gamma = \frac{\varepsilon_c}{C_{IX}} = \frac{a - a_0}{a_0 C_{IX}} \quad \text{(eq. 2)}$$

where a_0 is the equilibrium lattice constant of LLZO at $C_{IX} = 0$.

2.2: Molecular Dynamics simulations

Molecular Dynamics simulations were conducted to predict ~~the~~ well-averaged diffusion coefficients of both ~~the~~ Li^+ and the exchanged ion. To obtain a statistically accurate description ~~of~~ for the low concentration of exchanged ions, a larger 2x3x3 supercell with 3456 atoms was used. Thus, the structure has 18 and 36 exchanged ions for $C_{IX} = ¿$ 1.7% and 3.4%, respectively.

All classical MD simulations were conducted in the package DL_POLY 4.10 [60]. The polarizable Bush forcefield included the long-range Coulombic interaction and, the short-range Buckingham interaction with a core-shell model for the Oxygen atoms. The forcefield parameters for the Li-O, Zr-O, La-O were obtained from [1, 17], while the initial Na-O, Ag-O K-O parameters were obtained from [61] respectively, and re-fitted using DFT sampling results. The parameters and the goodness of the fit between the MD and DFT calculations are provided in **Table SI.1** and **Figure SI.1** respectively.

The MD protocol used an NVT ensemble with a Nosé thermostat set to 0.1 ps, and an equilibration run for 1 ps, and a timestep of 0.75 ps. MD trajectories were generated for 1.5 ns for temperatures in the range of 1200 to 900 K at 100K intervals. To evaluate the stress-diffusion coupling, the cell parameters were varied such that the hydrostatic strain corresponds to +1%, 0%, -1% and -2% (with plus representing compressive strain).

2.3: Continuum modelling of concentration and biaxial residual stress profiles

The Ion exchange process at elevated temperature was considered assumed on both sides of the electrolyte (2-sided exchange). and tThe resulting concentration profiles of the ion exchanged ions varying with position x (perpendicular to the plane of the electrode – electrolyte) and time t can be modelled based on the flux equation

$$\frac{\partial C_{IX}}{\partial t} = \frac{\partial}{\partial x} D_{IX} \text{¿} \qquad \text{(eq. 3)},$$

For the thickness L of the electrolytete , fixed surface concentration boundary conditions were used, assuming a large molten salt bath.

$$C_{IX}(x=0, t) = C_s$$

$$C_{IX}(x=L, t) = C_s$$

The resulting compressive stress profile $\sigma_C(x, t)$ is obtained by solving the mechanical equilibrium equation with plane strain boundary conditions

$$\sigma_C(x,t) = \frac{E\gamma\, C_{IX}(x,t)}{1-\nu} - \frac{E\gamma}{1-\nu}\int_0^L C_{IX}(x,t)\,dx$$

(eq. 4)

Where E is the Young's modulus of LLZO taken as 150 GPa [33], and ν is the Poisson's ratio taken as 0.257 [13]. The right-hand side of **eq.4** contains two terms; the first term is the biaxial compressive stress generated due to ion exchange and the second term is the averaged stress relaxation by the resulting tensile stress due to force balance. The tensile stress term is averaged over the concentration profile. [What about the tensile stress in the bulk material? Doesn't that play a role?]

A simplification can be made by neglecting the tensile stress term of **eq. 4** when solving **eq. 3** [32]. This is justified because the magnitude of the tensile stress is at least an order of magnitude lower than the compressive stress. [But the integrated tensile stress through the whole pellet is equal to that of the compressive stress, no?] Thus $\sigma_c(x,t)$ $\frac{E\gamma\, C_{IX}(x,t)}{1-\nu}$ is substituted in **eq.3** to express all the terms as a function of $C_{IX}(x,t)$, as

$$\frac{\partial C_{IX}}{\partial t} = \frac{\partial}{\partial x} D_{IX} ¿$$

which can be reduced to:

$$\frac{\partial C_{IX}}{\partial t} = \frac{\partial}{\partial x} D_{IX}(T, C_{IX}(x,t)) \frac{\partial C_{IX}}{\partial x}$$ (eq. 5)

Eq. 5 was solved at a constant temperature (typical for ion-exchange process), using the finite differences method and the resulting concentration profile was substituted into **eq.4** to obtain the stress profile.

For the fracture toughness evaluation, existing surface flaws were treated as a crack of length α, and modelled as sharp Griffith type crack failing in mode I. The apparent fracture toughness K_1 was written as

$$K_1(t) = ¿\sigma_{permissible} \vee Y\sqrt{\pi a} - \frac{Y 2\sqrt{a}}{\pi}\int_0^a \frac{\sigma_c(x,t)}{\sqrt{a^2 - x^2}}\,dx \qquad \text{(eq. 6)}$$

where Y is the shape factor taken as 1.12, $¿\sigma_{permissible} \vee ¿$ is the maximum tolerable tensile stress at the tip of a crack of length a [25, 32, 62].

3: Results and Discussions

3.1: Site selectivity of Exchanged Ions

Figure 2: Site selectivity of the larger exchange ion showing preference for octahedral sites. The configurations in which the Li^+ was exchanged out of an octahedral site are marked as 'O', tetrahedral are marked with a 'T'. The * marked configurations indicate ionic hopping by the exchange ion from tetrahedral to an octahedral site upon ionic relaxation.

Li^+ ions in LLZO prefer tetrahedral sites over octahedral sites by ~0.2 eV [52, 63]. This is because the Li-O bond distance in tetrahedral site (1.94 Å) is closer to the native Li-O bond distance in Li_2O (2.02 Å in the Fm-3m structure), compared with the Li-O bond distance in the octahedral site (2.27Å). To understand the site selectivity of the exchange ions, we perform the following DFT calculations. One Li^+ is exchanged with one exchange ion in the DFT simulation

box. 21 different Li^+ were chosen; 14 in the octahedral site, 7 in the tetrahedral site. For a particular exchange cation, one of the 21 cases has the minimum energy. This structure is used a reference state to compare the site occupancy energies, defined as ΔE_f. **Figure 2** shows the distribution of ΔE_f for the three exchange ions, Na^+ exchange is shown in green triangles, Ag^+ in orange squares and K^+ in navy circles. On the horizontal axis, the exchange with Li^+ originally in an octahedral site is shown as O, while the exchange with Li^+ originally in the tetrahedral site as T. * marked T configurations (*T1, *T2, *T3) are configurations in which the exchange ion was initially set in a tetrahedral site, however upon ionic relaxation, hops into an octahedral site. **Figure 2** reveals that for all three exchange cations, the lowest energy is an octahedral configuration (O13). Exchange ions stuck in tetrahedral configurations (T4-T7) have higher energy compared to Octahedral cases and can lower their energies by hopping into a neighboring empty octahedron (*T1-*T3). This behavior can be understood by comparing the exchanged ion-O bond length in the native oxides. Na-O bond length in Fm-3m Na_2O (2.42 Å), K-O bond length in Fm-3m K_2O (2.80 Å) and the Ag-O bond length in Pn-3m Ag_2O (2.09 Å) are larger than the allowable bond length in the tetrahedral site (1.94 Å).

3.2: Defect formation energy and precursors for Ion Exchange

Taking the lowest configuration in **Figure 2**, the ion exchange formation energy, E_f, depends on the reference state from which the exchanged ion is brought in, thus becoming precursor dependent. Consider the simple exchange reaction (**eq. 7**) in which IX represents the set of exchange ions [Na^+, Ag^+, K^+] while M represents the set of anions [SO_4^{2-}, O^{2-}, N^{3-} ….]. M may even be the metallic state (i.e. absence of any anions).

$$Li_7La_3Zr_2O_{12} + \delta IX - M \Leftrightarrow Li_{7-\delta}IX_\delta La_3Zr_2O_{12} + \delta Li - M \qquad \text{(eq. 7)},$$

Following the definition of **eq. 1**, **Figure 3** shows the E_f with different cation sources. The trend of exchanging Li^+ with K^+ and Li^+ with Na^+ appears similar. This is because Li^+, Na^+ and K^+ belong to the same alkali metal column and have similar crystalline structure in most of their commonly existing salts. The trend is different for the case of exchanging Li^+ with Ag^+, which usually has a different crystallization structure from the salts containing Li^+.

Within the dilute defect limit, the concentration of exchanged species may be approximated as $C_{IX}\ e^{\frac{-E_f}{RT}}$. Assuming the ion exchange occurs at 1200K for sufficient exchange ion mobility (discussed in section 3.4), it can be estimated that E_f ~ 0.3 eV would provide a concentration of ~ 5%, which is required to obtain biaxial residual stress of 1GPa (discussed in section 3.5). Negative E_f, suggesting corrosive (spontaneous) ion exchange reaction, is not recommended. These criteria allow us to screen precursors based on quick DFT calculations. For the exchange with Na^+, Na_3PO_4 (E_f = 0.29 eV), NaF (E_f = 0.45 eV) may be used. We add Na_2O (E_f = -0.03 eV) to the list as the E_f is only mildly negative. For the exchange with Ag^+, $AgNO_3$ (E_f = 0.27 eV), Ag_3PO_4 (E_f = 0.22 eV) may be used. For exchange with K^+, the E_f for all salts is higher than 1eV and hence the thermal driving force may not yield sufficient K^+ concentration, requiring additional driving forces. One such driving force is the oxygen gas release [18] by using KO_2 as a precursor to yield $Li_2O + O_2(g)$ after ion exchange.

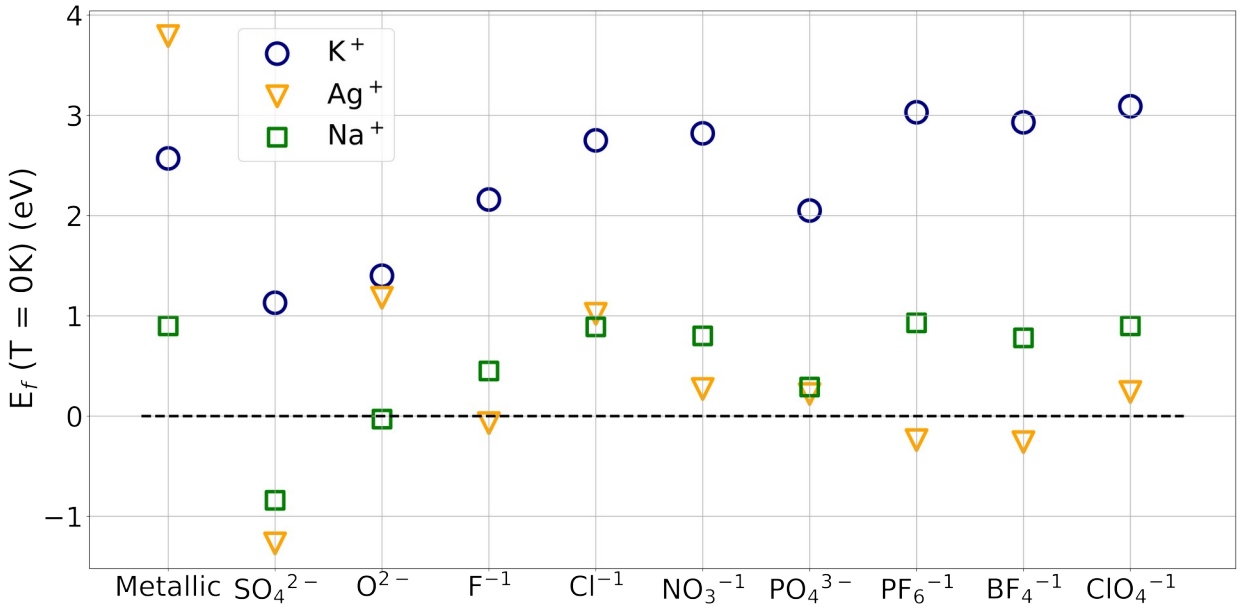

Figure 3: Variation of the defect formation energy E_f with different salts. The list of cations is shown in the legend navy for K^+, orange for Ag^+, green for Na^+, while the list of anions is shown along the horizontal axis. Black dashed line marks the line of spontaneous reactions, salts below this line are corrosive and salts above may be activated by temperature.

Next, we investigate if the dilute assumption is still valid up 5.1% by evaluating E_f at 3 different C_{IX} as shown in **Figure SI.2**. For simplicity, the reference state chosen was the native metal. The E_f varies less than 0.025 eV ~~by~~ per percentage change of C_{IX} for Na^+, Ag^+ and K^+ respectively, which we ~~conclude~~ take as low. Thus, dilute approximation can be assumed for IX formation energy, at least up to $C_{IX}=5\,\%$.

3.3: Free Expansion Coefficient, γ

Assuming exchanged ions are dilute, the chemical strain should increase linearly with the concentrations of ion exchange. This was confirmed by analyzing the freely expanded lattice constant (a) of ion exchanged LLZO with all three cations, shown in **Figure 4(a)**. The corresponding ~~chemical~~ chemical-~~strain~~ strain-derived free expansion coefficient (γ) was computed according to (**eq. 2**) and the comparison of γ against the size of three exchange ions and Li^+ in a 6-fold coordination is shown in **Figure 4(b)**. The dashed line is a linear fit between the ion size and γ, showing that the fit is linear (R^2 = 0.995). Thus larger exchange ions cause larger chemical strain in LLZO and the magnitude of the strain increases linearly. As a reference we provide the strain at 3.4% of each exchanged ion, as Na^+ ~2.38×10^{-3}, Ag^+ ~ 3.8×10^{-3} and K^+ 5.94×10^{-3}.

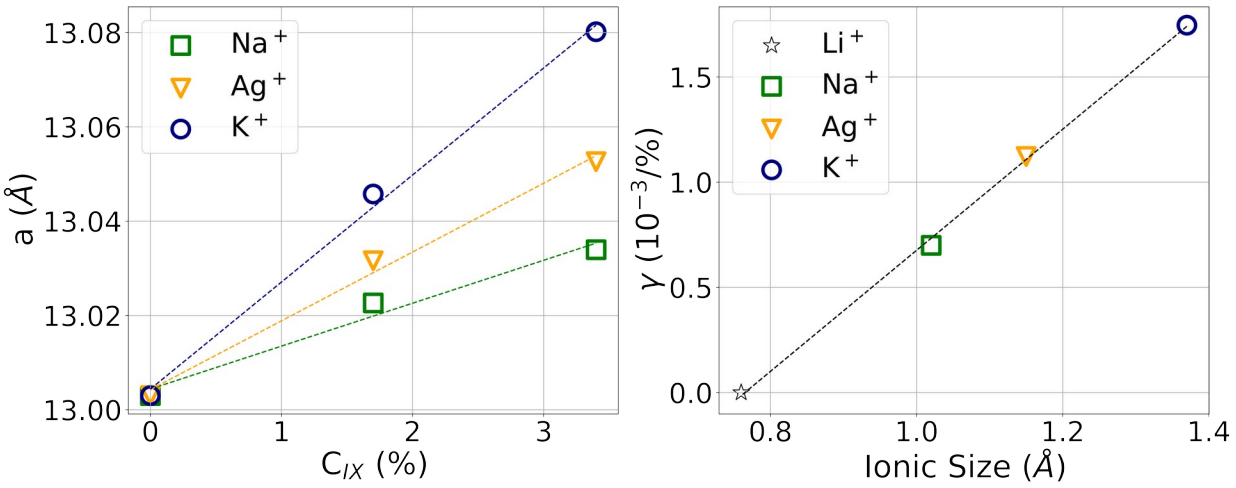

Figure 4: Linearly varying chemical strain due to ion exchange. (a) Freely expanded lattice constant (a¿ against the concentration of exchanged ion. Dashed lines represent the linear fits. (b) Variation of the free expansion coefficient (γ) against the size of the exchange ion in a 6-fold coordination. Dashed black line is a linear fit between γ and the ion size. Note that the trivial case of the zero expansion by exchanging Li^+ with Li^+ has been shown as black star.

3.4: High Temperature Mobility of Ion Exchange species in LLZO

To generate residual ~~in~~ in-plane compressive stresses in subsurface LLZO, the ~~exchanging~~ exchanged ions need to diffuse into the LLZO. Experimentally, the ion exchange process would be carried out at an elevated temperature such that the high temperature promotes exchanging and diffusion of ions to set up the concentration profile. Once the desired profile is set, the system can be cooled down to ~~lock~~ freeze this profile as the exchange ions are immobile at room temperature. To investigate the behavior of the ~~exchanging~~ exchanged ions at such temperatures, MD simulations were conducted at temperatures from 900 to 1250K. Higher temperatures would enter the sintering regime of LLZO [64-66] and hence were avoided; lower temperatures cause insufficient hopping of the exchanging ions (see **Figure SI.4.a, b**) within the time of our simulations, although they might be practical in real time.

We first discuss the behavior of the K^+ diffusion in LLZO at elevated temperature. DFT simulations at 0K suggest~~ed~~ that the exchanging K^+ defects are dilute until at a concentration of 3.4% ~~concentration~~. This was verified in MD simulations at 1.7% concentration where the MSD for K^+ increases linearly with time (**Figure SI.4c, Figure SI.5a**). However, at 3.4%, the MSD shows a plateau in the diffusion after ~600ps, where the K^+ ions hop aggressively in the beginning and end up clustered around each other as shown in **Figure SI.5b.** The clustering of K^+ at 3.4% depends on the temperature and stress in MD simulations. This was not captured at 0K DFT calculations but is consistent with the large IX formation energy leading to phase segregation. Therefore, K^+~~it~~ is no longer considered in the continuum models.

The trajectories of Na^+ and Ag^+ did not show clustering (within the simulation time). The MSD for Na^+ and Ag^+ in LLZO shows stress and C_{IX} dependence (**Figure SI.6a, b** for Na^+ and **Figure SI.6c,** ~~d for~~**d** for Ag^+). Although the defect formation energy and chemical strain follow the dilute limit at 0K based on DFT calculations, high temperature diffusion of ~~exchanging~~

exchanged ions may be more sensitive to the exchanged ion concentration. The diffusion coefficients of the exchanged ions D_{IX} along with their stress magnitudes σ_c ~~was~~ were obtained from the output file of DL_POLY. If 1200K ~~was~~ were chosen as the ion-exchange process temperature, D_{IX} from the molecular dynamics simulations was fitted at 1200K as a function of stress and C_{IX} for Na^+ and Ag^+ as shown in **Figure 5.a** and **Figure 5.b** respectively, and further fitted (shown as black lines) to,

$$D_{IX}(T=1200\,K, \sigma_c, C_{IX}) = D_1\left(e^{\frac{-\sigma_c V^*}{1200R}}\right)\left(1-\frac{C_{IX}}{d}\right) \qquad \text{(eq. 8)};$$

where D_1 can be interpreted as a diffusional pre-factor, V^* is the activation volume (The activation volume represents the difference in volume between the initial state and the activated (transition) state of a diffusing particle as it moves through its environment.), and d may be interpreted as the Bardeen and Herring correlation factor, which accounts for the effect of correlated atomic jumps on the overall diffusion process. [67]. Positive σ_c values are for compressive stress. The values for the fitting constants are provided in **Table 1**. It is noted that D_1 for Na^+ is higher than Ag^+ by almost a factor of 2 and thus Na^+ diffuses faster than Ag^+ in LLZO. Both Na^+ and Ag^+ have similar activation volumes thus requiring a similar amount of hydrostatic volume for a hop [68]. **The fitting factor *d* can be interpreted as the change in the diffusivity due to the concentration**. In the context of the mixed alkali effect, the exchanged ions behave like a dilute impurity in the diffusion network of Li^+ in LLZO and hence the diffusion exhibits concentration dependence. Since ~~in our fitting form,~~ d is in the denominator, larger values of d represent less sensitivity to concentration. As the d value for Na^+ is less than Ag^+, Na^+ has higher sensitivity to concentration than Ag^+.

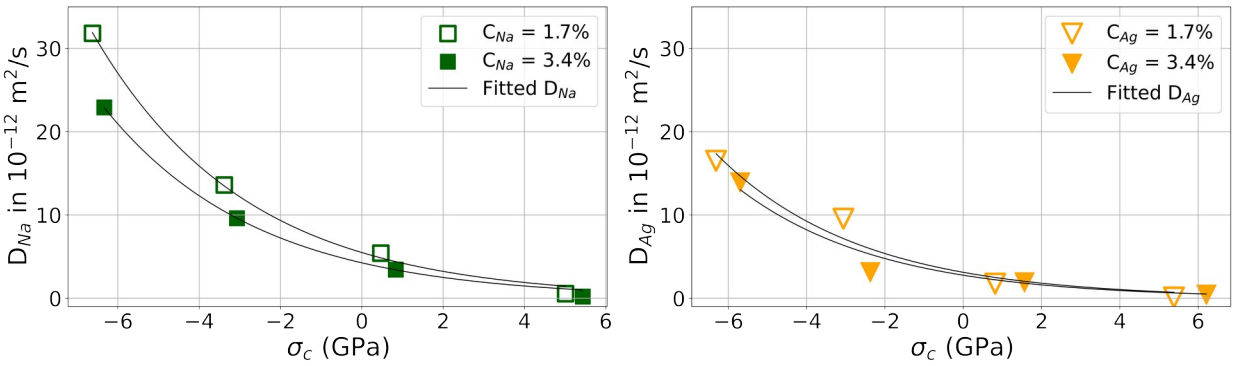

Figure 5: Showing the MD obtained and fitted diffusion coefficients for Na^+ (left panel) and Ag^+ (right panel) at T = 1200K. Open boxes represent 1.7% concentration and filled boxes represent 3.4% concentration. The fitted diffusion curve is shown in black

Table 1: Fitting parameters for the stress-concentration dependent diffusion expression for Na^+ and Ag^+ at 1200K.

Parameter	Na^+	Ag^+
D_1 (m^2/s)	6.73×10^{-12}	3.47×10^{-12}
$V^{¿}$ (m^3)	26.49×10^{-07}	27.13×10^{-07}
d (%)	9.25	16.90

3.5: 1D Continuum Model for the concentration and stress profiles

~~To use the free expansion coefficient) and the stress-concentration dependent diffusivity of the exchanging ions at 1200K (❑❑) in the continuum model and t~~The exact expression ~~of~~ for $D_{IX}^{1200\,K}\left(C_{IX}(x,t)\right)$ used in **eq. 5** is the following, with the parameters in **Table 1**.

$$D_{IX}^{1200\,K}\left(C_{IX}(x,t)\right) = D_1\left(e^{\frac{-\left(\frac{E\gamma\, C_{IX}(x,t)}{1-\nu}\right)V^{¿}}{1200\,R}}\right)\left(1-\frac{C_{IX}(x,t)}{d}\right) \qquad \text{(eq. 9)}$$

~~The~~ $D_{IX}^{1200\,K}$ was used as input in ~~the~~ a 1D continuum model with fixed surface concentration C_s boundary conditions to obtain the ion exchange concentration profiles, C_{IX}¿) as a function of time and position as in **eq. 5**. The mechanical equilibrium condition converts the concentration profile to a stress profile, $\sigma_C(x,t)$, as shown in **eq. 4**. We further clarify that the continuum

modelling is only done for Na^+ and Ag^+ ~~due to the ruling out~~of clustering by ~~of~~ K^+ at high concentrations ~~by clustering~~.

First, we comment on the need to implement concentration gradients for accurate estimation of gain in fracture strength. Previously, we assumed a uniform concentration in a shallow exchange depth~~,~~ to estimate the compressive stress [18]. A comparison of this uniform concentration model with the concentration gradient model is shown in **Figure SI.7**. Both cases have identical total dopant amount and identical surface concentration, so the concentration gradient model has a deeper ion-exchange depth than the uniform concentration model. It is seen in **Figure SI.7c** that the uniform concentration model can predict the magnitude of the stress profiles reasonably well but underestimates the exchange depth. Furthermore, as shown in **Figure SI.7d**, it provides inaccurate gains in the fracture strength by overestimating the improvements w.r.t. bulk at shallow exchange depths and underestimating them beyond the shallow depth ~~by~~ because of abrupt truncation. Hence, we only use the concentration gradient model for further discussion.

Within the concentration gradient model, the exact magnitude of the compressive and resulting tensile stress depends on the temperature (T), time for diffusion (t), and the boundary condition C_s. t can be made dimensionless by scaling it to the time that the exchange ion takes to diffuse across the electrolyte (characteristic time τ) to achieve a constant concentration. For a 1 mm thick electrolyte pellet with two-sided exchange τ = 2x10^5 s (~2.3 days, consistent with L^2/D). The dimensionless time (t/τ) can be used along with dimensionless spatial coordinates (x/L) to develop dimensionless maps for Na^+ and Ag^+ as shown in **Figure SI.8a** and **Figure SI.8b**. The maps provide the concentration profile (right panel) and the resulting dimensionless compressive stress in the left panel (scaled to the intrinsic fracture strength of LLZO) with various surface concentrations and dimensionless time (t/τ) at 1200K. [Maybe these figures could be in the main manuscript? Especially since they are referred to twice in the next paragraph. They seem pretty interesting.]

We believe ~~that~~ a desirable ion exchange should be ~~bound~~ controlled by two factors shown in red in the dimensionless maps. The lower bound of ion exchange is determined by the exchange depth, which should be such that the compressive stress profile exists beyond the tip of

the crack. A schematic illustrating this is shown in **Figure 6.a**. Any exchange depth that does not entirely encapsulate the tip of the crack does not provide any benefit to crack resistance, since growth of a sharp crack (at the continuum level) depends on the magnitude of the stress at the tip of the crack [62]. In the case of LLZO, the crack sizes, a, are limited by the existing flaws (grain size, surface damage, pores etc.), which tend to be within the limit of 2-20 μm [69, 70]. Thus, in the dimensionless maps, the lower bound of exchange profiles is determined by the limiting dimensionless crack size a/L, shown as a red triangular notch in the left panels of **Figure SI.8a** and **SI.8b**. (For example, in a L=1 mm thick electrolyte pellet, this corresponds to a 40 μm depth, larger than the largest flaw size by a factor of 2). Effective ion exchange concentration profiles should exist beyond this red notch. The upper bound of ion exchange is determined by the resulting tensile stress in the bulk. There exists a maximum value of the tensile stress in the bulk equal to the fracture strength of LLZO at which it will spontaneously shatter [71]. The typical fracture strength of LLZO $|\sigma_f|=150$ MPa [33] and this is shown as a horizontal red line in the left panel of the dimensionless stress map (**Figure SI.8a**, **SI. 8b**) with a value of -1 (minus indicating tensile). The resulting maximum tensile stress in the bulk should be lower in magnitude than the fracture strength (graphically above value of $\sigma_c = -¿\sigma_f \vee ¿$). [I suppose this requires a minimum thickness of the pellet? Presumably, we'll need the flaw sizes to be sufficiently small, which may be engineered.]

Within the two bounds of ion exchange, the dimensionless maps show the different profiles for stress and concentration depending on the C_s. The C_s can be estimated using two strategies: rely on thermodynamic arguments or back calculate based on the desired stress magnitude. The thermodynamic argument is as follows. At the ion exchange temperature ~1200K, we find the precursor such that E_f $0.3\,eV$, which corresponds to a C_s~5% within the dilute defect approximation. The back-calculation method estimates the C_s from the desired stress on the surface (σ_C^0) by a simple approximation C_s $\frac{\sigma_C^0(1-\nu)}{E\gamma}$. The origin of this equation is ignoring the small tensile stress second term on the right side in the mechanical **eq. 4.** For a σ_C^0 of ~1GPa, the C_s for the Na^+ corresponds to 7% and for Ag^+ is 4.5%. [1 GPa is almost certainly way too high. Why not do the calculation for 200 MPa?] Choosing them as the C_s, L = 1mm,

t/τ=1.8x10^{-3}, the concentration profiles are shown in **Figure 6.b.** It is evident from **Figure 6.b** that the ion exchange depth is of the order of ~170 μm for Na^+ and ~ 140 μm for Ag^+, thus being comfortably greater than the lower bound of 40 μm (shown as red notch in **Figure 6.b**). The corresponding stress profile is shown in **Figure 6.c**. To verify the upper bound we check the generated tensile stress in the bulk. For the Na^+ exchanged LLZO the tensile stress in the bulk is -96 MPa and the Ag^+ exchanged LLZO is -76 MPa as shown in in **Figure 6.c**, which are both lower in magnitude than – 150 MPa (graphically above the red line in **Figure 6.c**) and hence within the upper bound.

Once the desired profile of ion exchange is obtained, the ~~apparent~~ expected gain in the fracture strength may be computed. A linear residual compressive stress was superimposed on the traditional Griffith's crack as in **eq. 6**. With a shape factor of 1.12 and K_{1C} 1 $MPa\,m^{1/2}$, the maximum tolerable tensile stress, defined as $\sigma_{permissible}$, can be plotted vs the dimensionless crack size a/L. ~~,~~ ~~t~~The results are shown in **Figure 6.d.** The black line is the line of native LLZO, showing $\sigma_{permissible}$ decreasing with increasing flaw size. The reported maximum tolerable tensile stress, $\sigma_{permissible}$ is about ~120 MPa in native LLZO with a typical grain size of 20-microns, which can be viewed as an intrinsic flaw size.

Any ion exchange in the surface layer should enhance the fracture toughness ~~than the pristine LLZO~~ since it can risk both spontaneous fracture from the center and non-total encapsulation of flaws. Thus, there exists a maximum theoretical improvement by ion exchange such that the depth of the exchange is set to the encapsulation depth (a/L) and the tensile stress arising in the center of the bulk is exactly the fracture strength ($\sigma_c = -¿\sigma_f \vee ¿$). This theoretical~~ly~~ maximum improvement case is shown in the solid red line. A theoretical improvement with a safety factor of 2, corresponding to $\sigma_c = -0.5 \vee \sigma_f \vee ¿$ in the center, is shown as the dashed red line. The range of safe and effective ion exchange is shown between this curve and the native LLZO as the gray region. The gain in apparent fracture strength for the stress profile shown in **Figure 6.c** for the Na^+ and Ag^+ after the same scaled diffusion time but different surface concentrations, are shown as the colored lines. Considering the same intrinsic flaw size in a 1 mm LLZO sample (a/L=0.02), the maximum tolerable tensile stress, $\sigma_{permissible}$ increases to ~520 MPa with ion exchange using 1 GPa surface compressive stress. Thus, the gain in fracture

strength is ~ 400 MPa (a factor of ~3.33 times with respect to native LLZO). The gain in fracture strength is ~~dopant~~ dopant-~~size~~ size-dependent if identical surface concentrations are set for Na^+ and Ag^+. For example, in case the surface conditions are set such that $C_s = 5\%$, L = 1mm, and t/τ=1.8x10^{-3}. The maximum tolerable tensile stress using Na^+ is ~400 MPa while that with Ag^+ is larger ~565 MPa due to the larger chemical strain. Thus, this model can be used to design the ion-exchange process to obtain the ion-exchange concentration profile for the ideal fracture strength gain.

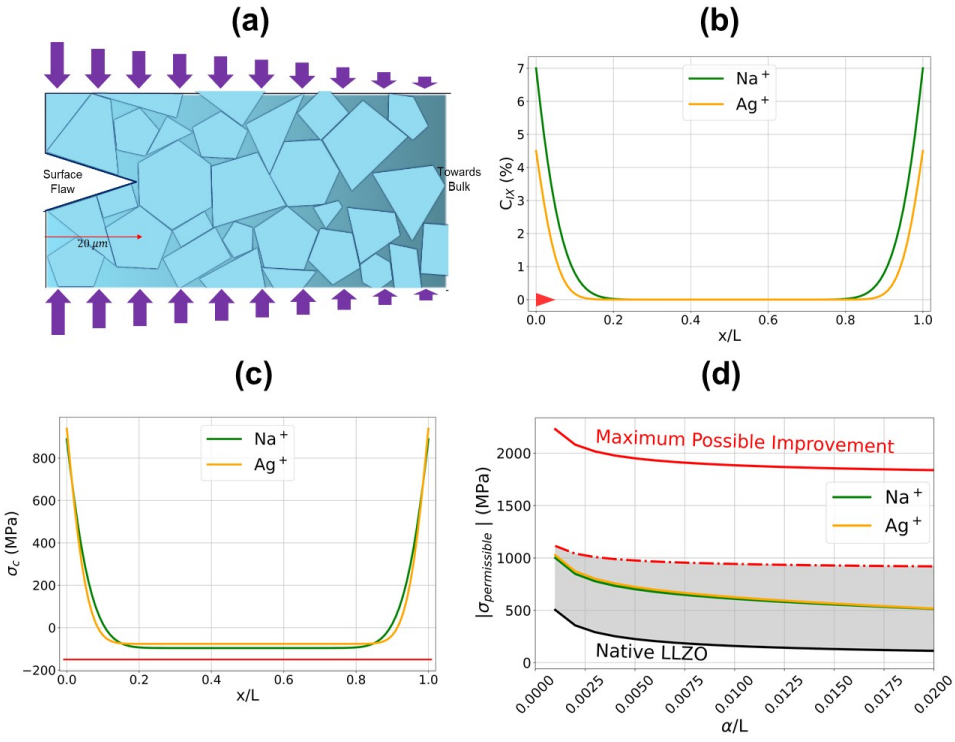

Figure 6: Showing the spatial continuum profiles of the concentration, stress and apparent fracture strength upon ion exchanging Na^+ and Ag^+ such that the surface stress ~ 1GPa at T = 1200K, at dimensionless time $\frac{t}{\tau}$ = 1.8x10^{-3}. (a) Schematic of the crack with a length of $\alpha = 20\,\mu m$ in a region with residual compressive stress. The gradient in blue is indicative of the magnitude of compression from bright (more compressive) to dark (less compressive). Purple arrows show the direction of the compressive stress field with respect to the crack (b) Concentration profile for the two side exchange using Na^+ and Ag^+ (c) Showing the resulting stress profile. The native fracture strength of LLZO - ¿σ_f∨¿ is shown as the red horizontal line (d) Showing maximum tolerable tensile stress (¿$\sigma_{permissible}$∨¿) at the tip of crack for crack propagation against the dimensionless crack size α (normalized to L). Black line shows the native LLZO, solid and dashed red line shows the maximum

possible improvement due to ion exchange, and the improvement with a safety factor of 2. Gray region shows the engineering range of improvement using the ion exchange approach.

3.6: Effect on Lithium mobility due to ion exchange

Ion exchange on the one hand can induce residual compressive stress in the ion exchanged region; however, on the other hand, direct insertion of exchanged ions in the Li^+ conduction pathways can have adverse effects on Li^+ mobility and eventually reduce diffusivity. These effects were investigated by a two-step fitting approach to extrapolate the diffusion coefficient of Li^+ at any temperature and stress based on MD simulations at higher temperatures and finite stresses using:

$$D_{Li}(T,\sigma_c) = D_0 e^{\frac{-\sigma_c V^{¿}}{RT}} e^{\frac{-E_a}{RT}} \qquad \text{(eq. 10)}$$

where D_0, $V^{¿}$, E_a are the diffusional pre-factor, activation volume and the activation energy respectively. T, σ_c are the fitting temperature and stress and R refers to the gas constant. The two-step fitting procedure for Li^+ was conducted akin to our previously reported approach in [18, 68]. The exchanged ion concentration remains low compared to the Li ion concentrations, thus D_{Li} is not sensitive to Li concentrations nor exchanged ion concentration.

Four benchmarks were used to investigate the change in diffusivity of Li^+ (**eq. 10**): the diffusional pre-factor (D_0), the activation volume ($V^{¿}$), the activation energy (E_a), which were extrapolated to room temperature and zero stress (D_{Li}¿). The results are shown in **Figure 7** which compares the fitting parameters for the diffusion of Li^+ in the three exchanging ions at different concentrations (1.7%, 3.4%) with the native LLZO. The unfilled green squares for Na^+ at 1.7% and filled green squares for 3.4% concentration. Orange triangles for Ag^+ at 1.7% shown in unfilled boxes and filled triangles for Ag^+ at 3.4% concentration and navy circle for K^+ at 1.7% concentration. The results for K^+ at 3.4% are not displayed due to the clustering effect. The dashed line represents the bulk Li^+ value in LLZO.

Figure 7a shows the activation volume of the Li^+ in ion exchanged LLZO. The positive activation volume means compressive stress will slowdown Li^+ diffusion. The general observation is that the activation volume of Li^+ increases with the size of the exchanged ion. This

is because larger exchanged ions exert a larger local compressive stress on the nearby mobile Li^+ which needs to overcome a larger local active volume for the same hops observed in native LLZO. We also draw attention to the magnitude of the activation volume of Li^+ being about 4 times less compared to the exchange ions (shown in **Table 1**); this is intuitive as Li^+ would require less volume compared to the exchange ions. However, the ratio is not proportional to the exchanged ion size since the bottlenecks of diffusion pathways in LLZO (the triangular face shared between the octahedral and tetrahedral Li^+ sites) are optimized for Li^+ and not the larger exchanging ions.

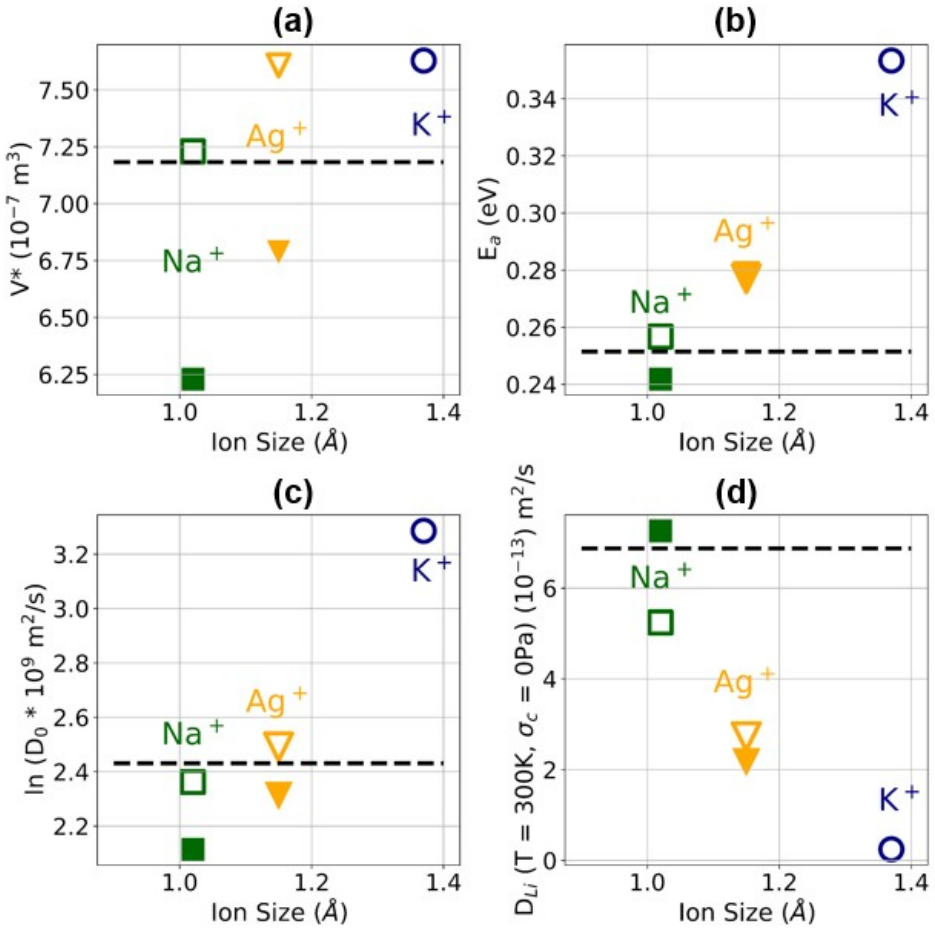

Figure 7: Comparison of the fitting parameters for the diffusion of Li^+ in the ion exchanged LLZO and bulk LLZO against the size of the exchanging ion. Green squares for the Na^+, yellow triangles for Ag^+, navy circles for K^+ and dashed black line for bulk LLZO. Open boxes represent 1.7%, and filled boxes represent 3.4% concentration. (a) Comparison of the activation volume (b) Comparison of the activation

energy (c) Comparison of the natural logarithm of the diffusional pre-factor (d) Comparison of the extrapolated room temperature and zero stress Li^+ diffusivity

Figure 7b shows the activation energy of Li^+ diffusion increases almost linearly with the size of exchange ion. We first note that ion exchange with Ag^+ and K^+ increases the activation energy of Li^+. The larger exchange ions prefer the octahedral site, and disallow the Li^+ to use the closest tetrahedral sites around them. This causes a blockage in the diffusion pathway of Li^+. In the case of Ag^+, concentration seems to have no effect on the Li^+ diffusivity as both the activation energies are similar ~0.28 eV (on top of each other). On the other hand, exchange with Na^+ does not affect the diffusivity of Li^+ since the difference in the activation energy from the native LLZO is ~0.01 eV. This may be because of the smaller mismatch between the size of Li^+ and Na^+.

Figure 7c shows the natural logarithm of the diffusion prefactor increasing linearly with the exchanged ion size. This can be understood by the simple Meyer – Neldel rule [72], as the activation energy scales linearly with exchanged ion size.

Figure7d shows the extrapolated room temperature and zero stress diffusivity of Li^+ in ion-exchanged LLZO. The Li^+ diffusivity drops linearly with the exchange ion size. For the case of Na^+ there is a negligible drop in diffusivity, for Ag^+ the diffusivity drops by 40% and with K^+ the drop is ~90%. However, we note that the drop is less than one order of magnitude with respect to the bulk for Na^+ and Ag^+. Even under the maximum compressive stress shown in **Figure 6.c** of ~1 GPa, the diffusivity drops by 24% thus still staying within the order of magnitude. Thus, ion exchange is suitable as it does not penalize the diffusivity of Li^+ significantly.

In the context of the mixed alkali effect, we do see an ion size dependent decrease in the diffusivity of the Li^+ in ion-exchanged LLZO, where the larger ions causing a larger decrease. We attribute this decrease primarily to the increase in the activation energy due to creation of blockage in the diffusional network of Li^+ caused by the larger exchanging ions.

3.7: Effect on the electronic ~~property~~ properties from~~after~~ ion exchange

Solid state electrolyte batteries require the electrolyte to be an insulator, which is true for the case of native LLZO (electronic bandgap for bulk LLZO ~ 4eV). Ideally, ion exchange must not alter the electronic band structure of these wide bandgap materials. This was confirmed by analyzing the electronic density of states occupation with ion exchange for the three exchange ions at 1.7% concentration from DFT calculations shown in **Figure SI.9**. The total electronic density of states is shown as a dashed navy curve representing the K^+ exchange, dashed orange for Ag^+, dashed green for Na^+ and solid black for bulk LLZO. No changes were observed for the K^+ and Na^+ exchange with respect to the LLZO. This is unsurprising as alkali metal ions do not have any unpaired electrons, and the bonds formed by the alkali – oxygen are of the alkali s – and Oxygen p orbitals which are similar for Li^+, Na^+ and K^+. On the other hand, the case of Ag^+ exchange is interesting as it introduces isolated defect states close the VBM as discussed in [19]. ~~Thus~~Thus, the size of the exchanging ion has no effect on the electronic band structure but the effects arise due to the nature of the transition metal electrons vs alkali metal electrons. [Is this a problem?]

4: Conclusion

The electro-chemo-mechanical failure of an all-solid-state battery at the~~ly degrading~~ Lithium metal anode | solid state electrolyte interface may be ameliorated by inducing residual compressive stress. Ion-exchanged induced surface residual compressive stresses in LLZO was modelled by a fully integrated multiscale modelling approach. The size effects of isovalent ions Na^+, Ag^+ and K^+ exchanging at ~~the~~ Li^+ sites in LLZO were investigated. Using DFT calculations, it was confirmed that ~~the~~ larger ions show a preference to inhabit ~~the~~ larger octahedral sites. Based on defect formation energies, promising precursors for driving Na^+ ion exchange can be Na_3PO_4, NaF or possibly Na_2O, while Ag_3PO_4, $AgNO_3$ are identified as Ag^+ sources. DFT calculations were also used to calculate the free expansion coefficient due to ion exchange and was found to increase linearly with the exchanged ion size.

Molecular Dynamics with the Bush polarizable force field was used to sample ~~more~~ exchanged ions due to their dilute concentrations. High temperature MD simulations reveal that

K^+ ions cluster ~~together~~ at 3.4% concentration, thus K^+ may be unsuitable for ion exchange. Na^+ and Ag^+ diffusion behavior at 1200 K was simulated and fitted to a stress~~,~~ - concentration ~~dependent~~ relationship, serving as input for continuum models. **In contrast, ~~the~~ Li-ion diffusion is less exchanged concentration dependent.** [I don't understand this sentence.] The activation volume and activation energy increase linearly with the exchanged ion size.

~~Microscale~~ A microscale two-side ion exchange process in 1 mm thick LLZO was simulated by continuum models with DFT and MD inputs. First, the ion exchange concentration profiles were simulated by solving Fick's law with the coupled stress and concentration dependent diffusion coefficient. Then the stress profile and the fracture toughness as a function of surface flaw size were predicted. The ~~necessity~~ value of this approach was highlighted by comparing the increase in apparent fracture strength against a previous assumed shallow doping and uniform concentration model. For the concentration gradient model, dimensionless maps exploring the concentration and stress profile with diffusion time were provided for the process of ion exchange. The lower bound and upper bounds of improvement in the fracture strength was discussed. Assuming a 1GPa desired surface stress, the concentration of Na^+ required was around 7% and 4.5% for Ag^+. The residual compressive stress field was superimposed on a linear elastic Griffith's type crack model indicating a gain of factor of 3.33 in the apparent fracture strength with ion exchange with respect to bulk (120 to 520 MPa) for a 20 μm surface flaw.

The stress-concentration coupled diffusivity of Li^+ was extrapolated to room temperature ~~at zero~~at zero and 1 GPa compressive stress. ~~However, t~~The drop in the Li^+ diffusivity is less than one order of magnitude with respect to the bulk of LLZO. In addition, investigation of the electronic density of states yields no change in the case of Na^+ and K^+ exchange with respect to bulk. ~~On~~ To the contrary, exchange with Ag^+ introduces isolated defects near the VBM which are localized to the Ag-O octahedral cage. Thus, ion exchange using Na^+ and Ag^+ is recommended as an effective strategy to induce residual compressive stress to ameliorate the electro-chemo-mechanically coupled cracking of LLZO | Lithium metal anode interface.

Supporting Information (SI)

The SI contains the Forcefield Parameters, Dilute defect assumption verification, Defect formation free energy, Diffusion of ion exchange species at high temperature, Comparison between the uniform concentration model vs. concentration gradient model, Dimensionless Maps for ion exchange using Na+, Ag+, and the Electronic density of states comparison.

Acknowledgement

The authors acknowledge the financial support from the Assistant Secretary for Energy Efficiency and Renewable Energy, Office of Vehicle Technologies of the U.S. Department of Energy (DOE) through the Battery 500 Consortium. S.J.H. was supported by the Assistant Secretary for Energy Efficiency, Vehicle Technologies Office of the U.S. Department of Energy under the Advanced Battery Materials Research Program.

References

1 M. Klenk, W. Lai, *Phys Chem Chem Phys* **2015**, *17*, 8758-68 10.1039/c4cp05690f.

2 R. Jalem, Y. Yamamoto, H. Shiiba, M. Nakayama, H. Munakata, T. Kasuga, K. Kanamura, *Chemistry of Materials* **2013**, *25*, 425-430 10.1021/cm303542x.

3 Y. Zhu, J. G. Connell, S. Tepavcevic, P. Zapol, R. Garcia-Mendez, N. J. Taylor, J. Sakamoto, B. J. Ingram, L. A. Curtiss, J. W. Freeland, D. D. Fong, N. M. Markovic, *Advanced Energy Materials* **2019**, *9*, 10.1002/aenm.201803440.

4 B. Gao, R. Jalem, Y. Tateyama, *ACS Appl Mater Interfaces* **2020**, *12*, 16350-16358 10.1021/acsami.9b23019.

5 H.-K. Tian, B. Xu, Y. Qi, *Journal of Power Sources* **2018**, *392*, 79-86 10.1016/j.jpowsour.2018.04.098.

6 T. Thompson, S. Yu, L. Williams, R. D. Schmidt, R. Garcia-Mendez, J. Wolfenstine, J. L. Allen, E. Kioupakis, D. J. Siegel, J. Sakamoto, *ACS Energy Letters* **2017**, *2*, 462-468 10.1021/acsenergylett.6b00593.

7 E. Kazyak, R. Garcia-Mendez, W. S. LePage, A. Sharafi, A. L. Davis, A. J. Sanchez, K.-H. Chen, C. Haslam, J. Sakamoto, N. P. Dasgupta, *Matter* **2020**, *2*, 1025-1048 10.1016/j.matt.2020.02.008.

8 G. Li, C. W. Monroe, *Phys Chem Chem Phys* **2019**, *21*, 20354-20359 10.1039/c9cp03884a.

9 T. Krauskopf, R. Dippel, H. Hartmann, K. Peppler, B. Mogwitz, F. H. Richter, W. G. Zeier, J. Janek, *Joule* **2019**, *3*, 2030-2049 10.1016/j.joule.2019.06.013.

10 H.-K. Tian, Z. Liu, Y. Ji, L.-Q. Chen, Y. Qi, *Chemistry of Materials* **2019**, *31*, 7351-7359 10.1021/acs.chemmater.9b01967.

11 P. Barai, A. T. Ngo, B. Narayanan, K. Higa, L. A. Curtiss, V. Srinivasan, *Journal of The Electrochemical Society* **2020**, *167*, 10.1149/1945-7111/ab9b08.

12 C. D. Fincher, C. E. Athanasiou, C. Gilgenbach, M. Wang, B. W. Sheldon, W. C. Carter, Y.-M. Chiang, *Joule* **2022**, *6*, 2794-2809 10.1016/j.joule.2022.10.011.

13 L. Porz, T. Swamy, B. W. Sheldon, D. Rettenwander, T. Frömling, H. L. Thaman, S. Berendts, R. Uecker, W. C. Carter, Y. M. Chiang, *Advanced Energy Materials* **2017**, *7*, 10.1002/ aenm.201701003.

14 S. S. Shishvan, N. A. Fleck, R. M. McMeeking, V. S. Deshpande, *Acta Materialia* **2020**, *196*, 444-455 10.1016/j.actamat.2020.06.060.

15 D. Bistri, C. V. Di Leo, *Journal of the Mechanics and Physics of Solids* **2023**, *174*, 10.1016/j.jmps.2023.105252.

16 X. Zhang, Q. J. Wang, K. L. Harrison, S. A. Roberts, S. J. Harris, *Cell Reports Physical Science* **2020**, *1*.

17 Y. Qi, C. Ban, S. J. Harris, *Joule* **2020**, *4*, 2599-2608 10.1016/j.joule.2020.10.009.

18 H. D. Jagad, S. J. Harris, B. W. Sheldon, Y. Qi, *Chemistry of Materials* **2022**, *34*, 8694-8704 10.1021/acs.chemmater.2c01806.

19 T. C. X. Xu, G. McConohy , H. Jagad , Y. Yang , S. Wang , S. Lee, C. Melamed, E. Barks, E. Kaeli, L. Narun, Y. Cui, Z. Zhang, H.R. Lee, R. Xu, M. Wang, A Romana, A. Geslin, R. Sinclair, Y. Cui, Y. Qi ,W. Gu ,W. Chueh *ChemRxiv; doi:10.26434/chemrxiv-2024-hf4cq* **2024**.

20 X. Yao, E. Olsson, M. Wang, J. Wang, Q. Cai, N. Peng, R. Webb, Y. Zhao, *Small* **2022**, *18*, 2108124.

21 F. Flatscher, J. Todt, M. Burghammer, H. S. Søreide, L. Porz, Y. Li, S. Wenner, V. Bobal, S. Ganschow, B. Sartory, *Small* **2024**, *20*, 2307515.

22 A. Sharafi, C. G. Haslam, R. D. Kerns, J. Wolfenstine, J. Sakamoto, *Journal of Materials Chemistry A* **2017**, *5*, 21491-21504.

23 E. J. Cheng, A. Sharafi, J. Sakamoto, *Electrochimica Acta* **2017**, *223*, 85-91.

24 V. Belostotsky, *Journal of non-crystalline solids* **1998**, *238*, 171-174.

25 R. Gy, *Materials Science and Engineering: B* **2008**, *149*, 159-165.

26 V. Tyagi, A. K. Varshneya, *Journal of non-crystalline solids* **1998**, *238*, 186-192.

27 C. Mahmoud A.-E-L, A.R., *Journal of the American Ceramic Society* **1979**, *62*, 390-395.

28 V. H. Gunawan, M. Schafer, K. M. Weitzel, *Phys Chem Chem Phys* **2024**, *26*, 14430-14439 10.1039/d4cp00262h.

29 A. Talimian, G. Mariotto, V. M. Sglavo, *International Journal of Applied Glass Science* **2017**, *8*, 291-300.

30 A. Talimian, P. Scardi, V. M. Sglavo, *Journal of Non-Crystalline Solids* **2020**, *550*, 10.1016/j.jnoncrysol.2020.120390.

31 E. E. Shaisha, A. R. Cooper, *Journal of the American Ceramic Society* **2006**, *64*, 278-283 10.1111/j.1151-2916.1981.tb09602.x.

32 G. Macrelli, *International Journal of Applied Glass Science* **2017**, *9*, 156-166 10.1111/ijag.12291.

33 S. Yu, R. D. Schmidt, R. Garcia-Mendez, E. Herbert, N. J. Dudney, J. B. Wolfenstine, J. Sakamoto, D. J. Siegel, *Chemistry of Materials* **2015**, *28*, 197-206 10.1021/acs.chemmater.5b03854.

34 J. Isard, *Journal of Non-Crystalline Solids* **1969**, *1*, 235-261.

35 A. Rodrigues, S. Fearn, M. Vilarigues, *Journal of the American Ceramic Society* **2019**, *102*, 7278-7287 10.1111/jace.16665.

36 P. Maass, *Journal of non-crystalline solids* **1999**, *255*, 35-46.

37 R. D. Shannon, *Acta Crystallographica Section A* **1976**, *32*, 751-767 https://doi.org/10.1107/S0567739476001551.

38 E. K. Hyde, **1959**.

39 R. A. Bernhoft, *Journal of Environmental and Public Health* **2012**, *2012*, 460508 https://doi.org/10.1155/2012/460508.

40 S. Galván-Arzate, A. Santamaŕıa, *Toxicology Letters* **1998**, *99*, 1-13 https://doi.org/10.1016/S0378-4274(98)00126-X.

41 W. C. Labys, A. Achouch, M. Terraza, *Resources Policy* **1999**, *25*, 229-238 https://doi.org/10.1016/S0301-4207(99)00030-6.

42 Y.-T. Cheng, M. W. Verbrugge, *Journal of Applied Physics* **2008**, *104*.

43 R. Deshpande, Y. Qi, Y.-T. Cheng, *Journal of the Electrochemical Society* **2010**, *157*, A967.

44 R. Deshpande, Y.-T. Cheng, M. W. Verbrugge, *Journal of Power Sources* **2010**, *195*, 5081-5088.

45 T. K. Bhandakkar, H. Gao, *International Journal of Solids and Structures* **2011**, *48*, 2304-2309.

46 G. Macrelli, J. C. Mauro, A. K. Varshneya, *Journal of the American Ceramic Society* **2021**, *104*, 5599-5613.

47 A. K. Varshneya, *International Journal of Applied Glass Science* **2010**, *1*, 131-142 10.1111/j.2041-1294.2010.00010.x.

48 Y. Qi, H. Guo, L. G. Hector, A. Timmons, *Journal of The Electrochemical Society* **2010**, *157*, A558.

49 Y. Qi, S. J. Harris, *Journal of The Electrochemical Society* **2010**, *157*, A741.

50 Y. Bi, J. Tao, Y. Wu, L. Li, Y. Xu, E. Hu, B. Wu, J. Hu, C. Wang, J.-G. Zhang, *Science* **2020**, *370*, 1313-1317.

51 M. P. O'Callaghan, A. S. Powell, J. J. Titman, G. Z. Chen, E. J. Cussen, *Chemistry of Materials* **2008**, *20*, 2360-2369 10.1021/cm703677q.

52 M. Xu, M. S. Park, J. M. Lee, T. Y. Kim, Y. S. Park, E. Ma, *Physical Review B* **2012**, *85*, 052301 10.1103/PhysRevB.85.052301.

53 H. Xie, J. A. Alonso, Y. Li, M. T. Fernández-Díaz, J. B. Goodenough, *Chemistry of Materials* **2011**, *23*, 3587-3589 10.1021/cm201671k.

54 J. Hafner, G. Kresse, in *Properties of Complex Inorganic Solids*, **1997**, Chap. Chapter 10, pp. 69-82.

55 J. P. Perdew, K. Burke, M. Ernzerhof, *Physical review letters* **1996**, *77*, 3865.

56 A. Jain, S. P. Ong, G. Hautier, W. Chen, W. D. Richards, S. Dacek, S. Cholia, D. Gunter, D. Skinner, G. Ceder, K. A. Persson, *APL Materials* **2013**, *1*, 10.1063/1.4812323.

57 T. Das, J. D. Nicholas, B. W. Sheldon, Y. Qi, *Physical Chemistry Chemical Physics* **2018**, *20*, 15293-15299.

58 M. Varenik, B. Xu, J. Li, E. Gaver, E. Wachtel, D. Ehre, P. K. Routh, S. Khodorov, A. I. Frenkel, Y. Qi, *Nature Communications* **2023**, *14*, 7371.

59 D. Er, J. Li, M. Cargnello, P. Fornasiero, R. Gorte, V. Shenoy, *Journal of the Electrochemical Society* **2014**, *161*, F3060.

60 I. T. Todorov, W. Smith, K. Trachenko, M. T. Dove, *Journal of Materials Chemistry* **2006**, *16*, 1911-1918 10.1039/B517931A.

61 T. S. Bush, J. D. Gale, C. R. A. Catlow, P. D. Battle, *Journal of Materials Chemistry* **1994**, *4*, 831-837 10.1039/JM9940400831.

62 H. Tada, P. C. Paris, G. R. Irwin, *The Stress Analysis of Cracks Handbook*. Editor, ASME Press, **2000**.

63 X. He, Y. Zhu, Y. Mo, *Nat Commun* **2017**, *8*, 15893 10.1038/ncomms15893.

64 X. Huang, Y. Lu, Z. Song, T. Xiu, M. E. Badding, Z. Wen, *Journal of Energy Chemistry* **2019**, *39*, 8-16 10.1016/j.jechem.2019.01.013.

65 Y. Gong, Z.-G. Liu, Y.-J. Jin, J.-H. Ouyang, L. Chen, Y.-J. Wang, *Ceramics International* **2019**, *45*, 18439-18444 10.1016/j.ceramint.2019.06.061.

66 W. Xue, Y. Yang, Q. Yang, Y. Liu, L. Wang, C. Chen, R. Cheng, *RSC Adv* **2018**, *8*, 13083-13088 10.1039/c8ra01329b.

67 J. G. Mullen, *Physical Review* **1961**, *124*, 1723-1730 10.1103/PhysRev.124.1723.

68 M. J. Aziz, *Applied physics letters* **1997**, *70*, 2810-2812.

69 J. H. Cho, K. Kim, S. Chakravarthy, X. Xiao, J. L. M. Rupp, B. W. Sheldon, *Advanced Energy Materials* **2022**, *12*, 10.1002/aenm.202200369.

70 Y. Zhang, D. Hu, J. Deng, F. Chen, Q. Shen, A. Li, L. Zhang, S. Dong, *Journal of Alloys and Compounds* **2018**, *767*, 899-904 10.1016/j.jallcom.2018.07.174.

71 S. Karlsson, *Ceramics - Silikaty* **2017**, 188-201 10.13168/cs.2017.0016.

72 A. Dalvi, N. Parvathala Reddy, S. C. Agarwal, *Solid State Communications* **2012**, *152*, 612-615 10.1016/j.ssc.2012.01.018.